Far-field radar NDT technique for detecting GFRP debonding from concrete

Oral Büyüköztürk *, Tzu-Yang Yu

Department of Civil and Environmental Engineering, Massachusetts Institute of Technology, 77 Massachusetts Avenue, Room 1-280, Cambridge, MA 02139, USA

Available online 19 November 2007

Abstract

A radar nondestructive testing (NDT) technique using an airborne horn antenna operating in the far-field condition is developed for detecting damages such as debonding and concrete cracking in glass fiber reinforced polymer (GFRP)-wrapped concrete columns. The far-field airborne radar (FAR) NDT technique is advantageous for distant measurement in practical applications where contact/near-contact measurement becomes an issue. In this technique the radar antenna operates in inverse synthetic aperture radar (ISAR) mode. Laboratory measurements at the frequency range 8–18 GHz are made on artificially damaged GFRP–concrete specimens for a preliminary validation of this technique. Collected frequency–angle measurements are further processed by the fast backprojection algorithm to render range–cross-range imagery for damage detection. From the reported measurements and imaging results the proposed FAR NDT technique is conceptually validated; the potential of this technique is shown in identifying defects and debonding in the GFRP–concrete interface regions of the concrete columns wrapped with these composite materials.
© 2007 Elsevier Ltd. All rights reserved.

Keywords: NDT; Radar; GFRP-wrapped concrete columns; Backprojection algorithm; Delamination

1. Introduction

Fiber-reinforced polymer (FRP) composite jacketing systems have emerged as an alternative to traditional construction, strengthening, and repair of reinforced concrete columns and bridge piers. A large number of projects, both public and private, have used this technology and escalating deployment is expected, especially in seismically active regions. The American Concrete Institute (ACI) has compiled a comprehensive guide to address various design issues [1].

In a recent study [2], it was reported that in such a FRP–concrete system cracking or crumbling of concrete inside the FRP jacket, and/or debonding of the FRP layer from concrete could occur under various degrees of confinement pressure provided by the FRP jacket. Fig. 1 shows the local crumbling failure of concrete in a specimen with high level of confinement. High confinement level is often introduced for column strengthening purposes, should there be a change of functionality or a need to upgrade for seismic counter-measures [3,4]. This type of failure has also been observed in actual columns (Fig. 2). Fig. 3 shows a global shear crack failure of concrete in a specimen with relatively low levels of confinement. Low confinement level is provided using less amount of FRP fabrics. Both scenarios are equally common in industrial practices [6]. While various types of FRP are available, including aramid (AFRP), carbon (CFRP) and glass (GFRP), this paper only considers the strengthening of concrete columns using GFRP.

Existing damages in the interface vicinity, debonding of GFRP from concrete, debonding between layers of a GFRP wrap and those in overlap joints may lead to catastrophic failures at loading stages earlier than those corresponding to intact specimens. Although debonding is often accompanied by discoloring that can be detected by naked

---

* Corresponding author. Tel.: +1 617 253 7186; fax: +1 617 253 3479.
E-mail address: obuyuk@mit.edu (O. Büyüköztürk).

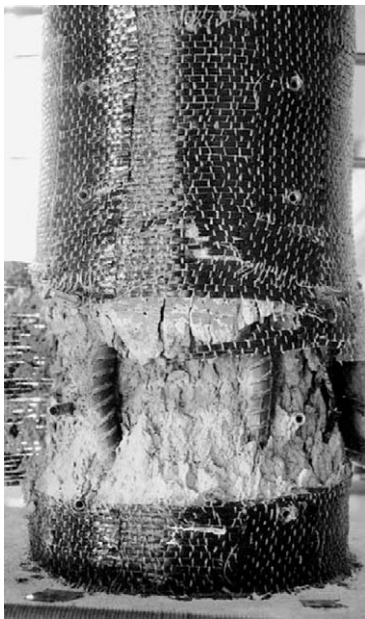Fig. 1. Local concrete crumbling [2].

Fig. 2. Column failure [5].

Fig. 3. Global shear cracking [2].

eyes [7], inner ply debonding may not show as well for multi-ply jacketing systems. Overlap joint length reduction due to progressive debonding during a seismic event may also be possible. Overlap joint failures have been reported in laboratory tests regardless of FRP configuration of the jacketing system [2,8]. All these failures can be associated with the onset of near-surface debonding within GFRP layers or between GFRP and concrete. Thus, near-surface debonding is used as a precursor for the damage detection in GFRP-wrapped concrete columns.

In this paper, we report the development of a radar NDT technique using an airborne horn antenna operating in the far-field condition for detecting near-surface debonding in GFRP-wrapped concrete columns. This technique aims at the visualization of near-surface debonding damages in GFRP-wrapped concrete columns for condition assessment. To validate the concept of this technique, far-field radar measurements are made on two artificially damaged GFRP–concrete specimens in the compact radar cross-section (RCS)/antenna range facility at MIT Lincoln Laboratory. The horn antenna operates in the inverse synthetic aperture radar (ISAR), and measurements at different frequencies and angles are collected. The frequency–angle data are further processed by the backprojection algorithm to render physical imagery of the structure for condition assessment. Two measurement schemes (normal and oblique) are identified and compared for their performance on damage detection.

This paper is structured in the following order: first, current NDT techniques are reviewed. The proposed FAR NDT technique is described by introducing the design parameters of radar. Experimental set-up and configuration of physical radar measurements are described, and the measurement schemes are explained. Principles of fast backprojection algorithm are then introduced, followed by the condition assessment based on frequency–angle data and range–cross-range imagery. Finally, research issues regarding future development of this technique are addressed.

2. Current NDT techniques

There is a need for an effective NDT technique that is capable of detecting and characterizing concrete anomalies and FRP debonding in a FRP-wrapped concrete system. Specifically, methods to detect: (1) the extent of concrete cracking, crumbling, and FRP debonding from concrete, (2) jacket debonding in the FRP–FRP interface, and (3) sizeable air pockets trapped between FRP and concrete during manufacturing are needed. Currently, several NDT techniques have been under investigation. They include stress wave (acoustic), infrared thermography, X-ray, and radar (microwave) techniques. Acoustic, infrared thermography, and radar techniques have recently been of particular interest to researchers for possible damage assessment of reinforced concrete and FRP-bonded concrete structures in laboratory settings [9–16].

2.1. Acoustic methods

Acoustic methods are based upon elastic wave propagation in solids. They include the techniques of pulse-echo, impact-echo, ultrasonic, acoustic emission, and spectral analysis of surface waves (SASW). Disadvantages include the need of intimate contact between the equipment and the subject, the use of sound couplant, as well as the existence of multiple paths through the same subject that make result interpretations difficult [17].

2.2. Infrared thermography

Infrared thermography is based on the detection of heat flow in the subject in which air gaps resulting from debonding act as insulators, which block out the proper heat flow. Data interpretation is, however, complicated because of varying ambient temperature conditions and surface emissivity variations, which is a function of surface properties [18]. An attempt was made by [16] to quantify subsurface damages of FRP-bonded concrete using infrared thermography.

2.3. Radiography

Radiography-based evaluation methods use high frequency electromagnetic radiation (X-rays and Gamma rays) or particular beams (beta rays and neutron radiation) passing through the subject and exposing it onto a film on the other side of the subject. Limitations include the need to access both sides of the subject, the need of safety precautions, long exposure, and two-dimensional (2D) images of three-dimensional (3D) subjects [19].

2.4. Microwave/radar technique

Microwave or radar has been used extensively for site characterization in geotechnical engineering. It has also been used to evaluate concrete structures, pavements, and bridge decks [18–22]. Radar involves the generation and transmission of electromagnetic waves into materials such as concrete with different dielectric constants [23,24]. Voids, delaminations, rebars, and material characteristics can be detected and interpreted from the reflected waves [25]. Optimization between penetration depths and detection capability, two inversely related parameters that are dependent on the frequencies and bandwidth of the wave, could be a challenge. Conventional radar often makes use of low frequencies to enhance penetration but with sacrificed detectability [26]. With the proper development of wideband, multi-frequency capability and tomographic imaging techniques, along with measurement of dielectric properties of the subject materials, however, radar can be a powerful tool in assessing structural members that consist of hybrid materials.

In spite of these developments, currently, there is no reliable technology capable of visualizing and characterizing various forms of GFRP-wrapped concrete damages without contact or near-contact inspection. The FAR NDT technique is developed mainly to overcome this obstacle, while providing desired levels of resolutions for different inspection purposes (e.g. preliminary and detailed inspections).

3. Far-field airborne radar (FAR) NDT technique

The proposed far-field airborne radar technique mainly consists of an airborne horn antenna, a signal generator, a signal modulator, and an analyzer. In principle, modulated radar signals or EM waves are designed and generated by the signal generator, modulated by the modulator, and transmitted by the horn antenna. The horn antenna is placed beyond the far-field distance from the target structure. Hence, the impinging EM waves on the structure will be essentially plane waves. Far-field measurement allows inspections from distance for highway and cross-river bridge columns. Furthermore, the waveform is mathematically simplified for signal processing. The far-field distance will be explained in this section.

Reflected EM waves or radar signals are collected by the same horn antenna and processed by the analyzer. The radar measurements are collected in ISAR mode; in other words, the reflected signals are received at different angles with respect to the structure. Image processing algorithms are then applied for processing the reflected signals and for forming the imagery as a basis for condition assessment.

In this section, important radar parameters including pulse width and bandwidth, range and cross-range resolutions, polarization, and radar cross-section (RCS) are first introduced. The difference between near-field and far-field is also defined.

3.1. The far-field distance

Antenna patterns vary in shape depending on the distance from the antenna, noted as R, and with the angular direction (polar distribution). In the case of a large distance from the antenna, the shape of the radiation pattern over a sphere of constant radius is independent of R. This distance or the Rayleigh distance is characterized and determined by the far-field condition. The far-field region is constituted by the distances exceeding the far-field distance, in which waves become plane. Thus, the target placed in this region is subject to plane waves. Mathematically, such region only occurs at infinity. Therefore, the use of the far-field distance in practice is always associated with finite error. A commonly accepted far-field condition in engineering is

$$R \geqslant \frac{2D^2}{\lambda} \qquad (1)$$

where D is the diameter of the smallest sphere that completely contains the antenna, and λ is the smallest wavelength of the transmitted wave [27]. The far-field distance is found when the equality of Eq. (1) is held, and is associ-

ated with a wave front error of 1/16 the smallest wavelength. For example, the far-field distance is approximately 4.7 m at 8 GHz, and 10.6 m at 18 GHz when $D = 0.3$ m.

3.2. Radar parameters

3.2.1. Pulse width and bandwidth

A linear frequency modulated waveform generated by radar consists of a rectangular pulse of duration $T = t_2 - t_1$ as shown in Fig. 4a. The carrier frequency f is swept over the pulse length by an amount B which represents the bandwidth, as shown in Fig. 4b. For the case of a modulated pulse length similar to T, the swept bandwidth and the achievable pulse are related by [28]:

$$T \cong \frac{1}{(f_2 - f_1)} = \frac{1}{B} \tag{2}$$

where f_1 and f_2 are the starting and ending frequencies, respectively.

3.2.2. Range and cross-range resolutions

Range resolution is defined on the radial (or range) distance from the radar to the target and is obtained from the transmitted signal. Cross-range resolution is related to the resolution perpendicular to the radial direction, and it is obtained by integrating the reflected energy from the target medium as the radar sweeps alongside the area of illumination. The relationships for the range and cross-range resolutions associated with radar are given by the following expressions, respectively [29]:

$$\rho_r = \frac{v}{2B} \tag{3}$$

$$\rho_{xr} = \frac{\lambda_c R}{2D} \tag{4}$$

where v = wave velocity, B = bandwidth, and λ_c = wavelength at center frequency. Eqs. (3) and (4) are the commonly accepted measure of resolution. Precise expressions are dependent on more specific definitions of resolution [30,31]. In a non-magnetic dielectric material (e.g. concrete) these resolutions are given by:

$$\rho_r = \frac{\left(\frac{c}{\sqrt{\varepsilon_r}}\right)}{2B} \tag{5}$$

$$\rho_{xr} = \frac{\left(\frac{c}{f_c \sqrt{\varepsilon_r}}\right) R}{2D} \cong \frac{\left(\frac{c}{f_c \sqrt{\varepsilon_r}}\right)}{2\theta_{int}} \tag{6}$$

where c = speed of light in free-space, ε_r = dielectric constant of the medium, f_c = center frequency, and θ_{int} = angular rotation of the target during processing time. For X- and Ku-band whose bandwidths are 4 and 6 GHz, respectively, the corresponding range resolutions in free-space are 38 and 25 mm. For $D = 0.3$ m and $\theta_{int} = 60°$, the cross-range resolutions in free-space are 0.014 m (X-band) and 0.009 m (Ku-band). These resolutions are smaller in dielectrics because the wavelength becomes shorter as indicated by Eqs. (5) and (6). Thus, damages or defects whose characteristic lengths are comparable to or greater than these values are theoretically detectable.

3.2.3. Polarization

Polarization is defined as the variations of the orientation of electric field with respect to time. Considering that the target under test is an infinite cylinder (treated as a two-dimensional structure), the incident field is referred to as VV-polarized or TM (transverse magnetic) when the electric field is parallel to the axis (infinite dimension) of the cylinder. The other polarization is referred to as HH-polarized or TE (transverse electric) when the electric field is perpendicular to such axis. In the two mentioned polarization options, if the orientation of the electric field does not change with increasing distance, then they are termed linear polarizations. Circular polarization, on the other hand, allows for the electric and magnetic field orientations to rotate about the direction of propagation with increasing distance. The availability of the HH and VV polarizations is a key advantage of radar methodologies for NDT applications on anisotropic materials whose properties are dependent on the direction of measurement.

3.2.4. Radar cross-section

Estimation of the signal strength received by a radar receiver requires the knowledge of the signal strength decay of transmitting waves, the response of reflected waves by a remote obstacle, and the dispersion of the reflected waves by the obstacle. A single function σ, referred to as radar cross-section (RCS) is usually used to characterize the far-field obstacle reflection. Formally, RCS is defined as:

$$\sigma = \lim_{R \to \infty} 4\pi R^2 \frac{|\bar{E}^{scat}|^2}{|\bar{E}^{inc}|^2} \tag{7}$$
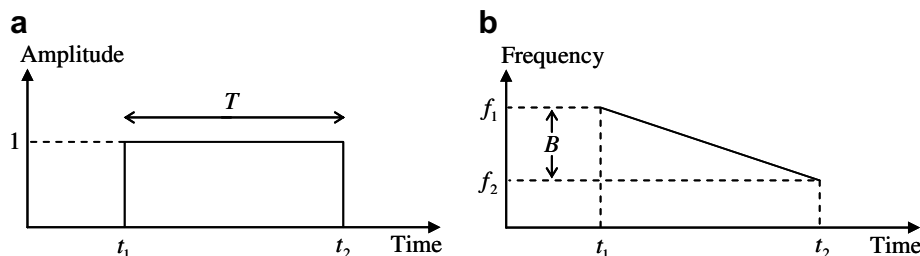

Fig. 4. Linear frequency modulated pulse waveform.

where $\bar{E}^{scat}$ and $\bar{E}^{inc}$ are the scattered and incident electric fields [32]. By its definition, RCS provides information about the target's characteristics and removes the effects of the transmitted power, receiver sensitivity, and the relative distance between the transmitter and receiver.

4. Physical radar measurement

The objective of the exploratory experimental program described in this section is the application of high resolution ISAR radar technologies for the detection and assessment of defect and damage features in GFRP-confined concrete specimens. The experimental set-up, description of test parameters, sample configurations, and data processing are discussed.

4.1. Experimental set-up and configuration

The radar measurements of GFRP-confined concrete specimens were performed at MIT Lincoln Laboratory using the Compact RCS/Antenna Range facility. The experimental set-up consists of a horn antenna, stepped-frequency radar and network analyzer systems, and a Harris Dual-Shaped reflection system, Model 1606, designed for conducting far-field studies. The purpose of this reflection system is to produce plane waves (far-field condition) in the limited space of laboratory. The reflection system is not necessarily required when applied in the field. A photograph of this experimental facility is shown in Fig. 5. The facility can achieve high signal-to-noise ratio measurements for a large frequency bandwidth ranging from UHF (0.7 GHz) to 100 GHz. This radar system is capable of producing a 20-m quiet zone, different antenna radiation patterns, and full polarimetric RCS measurements. The radar measurements are collected in monostatic mode in which only one horn antenna is used as transmitter and receiver. Specimens are placed on top of a Styrofoam tower that is capable of fully rotating the target at predetermined angular steps. The measurements were conducted in stepped-frequency mode by sweeping from a starting frequency f_1 to an end frequency f_2 in 0.02 GHz increments at a fixed angle. The target is then rotated to the next angular step and the frequency sweeping is again performed.

Radar measurements were conducted at X- and Ku-band frequencies (8–12 and 12–18 GHz, respectively) to achieve optimized resolution and surface penetration capabilities. The range resolution is directly related to the bandwidth of radar signals. The total rotation angle is 60° in the ISAR measurements and angular increments are 0.1° and 0.2. Two types of polarizations were used in the radar measurements: HH-polarization and VV-polarization. These measurements were collected in the far-field condition using the facility shown in Fig. 5.

While the resolution achieved in the radar measurements is significantly high, the trade-off is evident in terms of penetration capabilities. Using the definition of penetration depth for a non-magnetic, dielectric material, the penetration depth is controlled by the permittivity of the material and the measurement frequency. When dielectric losses occur in the material due to conduction currents, the equivalent conductivity σ is expressed as:

$$\sigma = \varepsilon_r'' \varepsilon_0 \omega \qquad (8)$$

where ε_r'' is the imaginary part of the complex permittivity, ε_0 is the permittivity of air (in free-space), and ω is the angular frequency.

The determined dielectric constant and loss factor using the proposed dielectric property characterization methodology [33] for concrete are 5.69 and 0.62, respectively. The estimated penetration depths are approximately 50
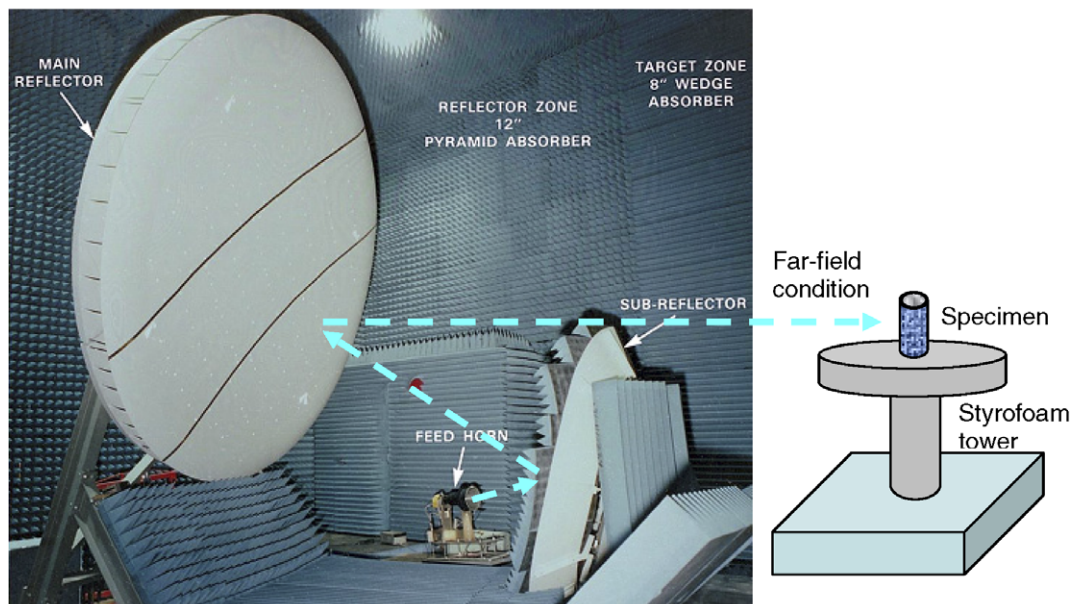

Fig. 5. Compact RCS/antenna range facility [Courtesy of MIT Lincoln Laboratory].

and 22 mm for 8 and 18 GHz frequencies, respectively. Although the use of high frequency radar waves results in shallow penetration depths, the proposed X- and Ku-bands were originally selected in view of the need to detect near-surface defects such as GFRP debonding from concrete and mechanical damage in the concrete regions close to the GFRP jacket.

4.2. Specimen description

Two artificially damaged GFRP-wrapped concrete cylinder specimens were prepared for physical radar measurements (Fig. 6). Artificial damages were introduced by insertion of Styrofoam elements (whose dielectric properties are same as air) on the surface of concrete cylinders, representing construction defect and GFRP delamination. The artificially damaged concrete specimens were then wrapped by GFRP sheet which adhered to concrete with epoxy. The average 28-day strength of the concrete was 26 MPa. The water-to-cement ratio was 0.45. In this paper we report preliminary results of measurements on specimens with artificial damages.

4.3. Measurement schemes

For radar measurements, the specimens under investigation were placed on top of a Styrofoam tower in two alternative orientations: (1) having the specimen rest on one of its ends, referred to as vertical position, and (2) having the specimen rest on its side, referred to as horizontal position. Schematics of the two measurement schemes are presented in Fig. 7. For the specimen with vertical orientation the incident angle θ varies on the x–y plane when the specimen rotates around the z-axis. Strong reflections are expected for all θ due to the specular effect. On the other hand, the incident angle φ varies on the y–z plane as the specimen rotates around the x-axis in the oblique incidence scheme. The specular effect is only significant when $\varphi = 90°$ in this monostatic mode configuration. For all other incidences, the incident wave meets the specimen in an oblique fashion. Both measurement schemes were designed to capture different EM wave scattering behaviors, and consequently, investigate their effectiveness when the far-field radar NDT technique is applied for damage or defect detection in GFRP-confined concrete structures.
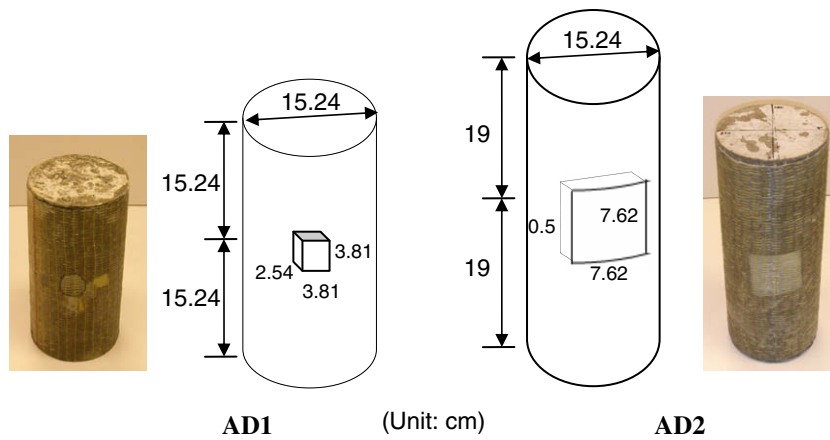

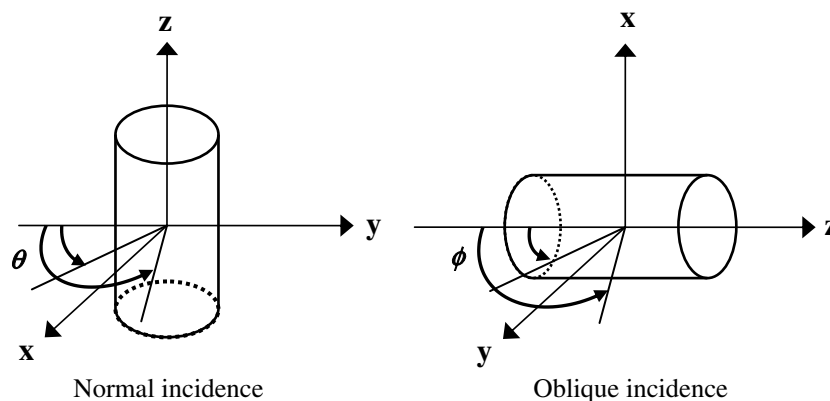Fig. 6. Two artificially damaged GFRP–concrete specimens.

Fig. 7. Normal and oblique incidence schemes.

4.4. Measurement results

The radar measurements were collected in ISAR mode, and they consisted of HH and VV polarization measurements as functions of frequency at fixed incident angles. For each polarization, an amplitude entry and a phase entry were recorded at each frequency step. Measurement results are processed and rendered in frequency vs. angle imagery as shown in Figs. 9–12. Only HH polarization (TE wave) measurements are reported in this paper since the differences in measurements between HH and VV polarizations were found to be insignificant. Fig. 8 shows the far-field radar measurements in HH polarization at X-band from intact (without defect) and damaged (with defect) surfaces of the specimen AD1 using normal incidence scheme. Fig. 9 shows the normal incidence measure-
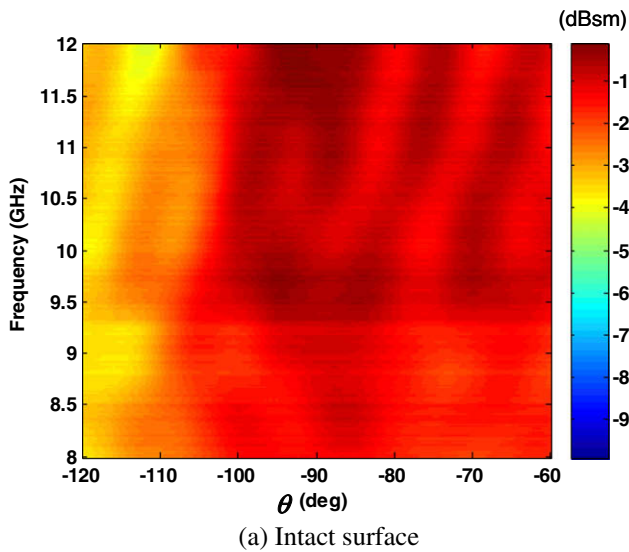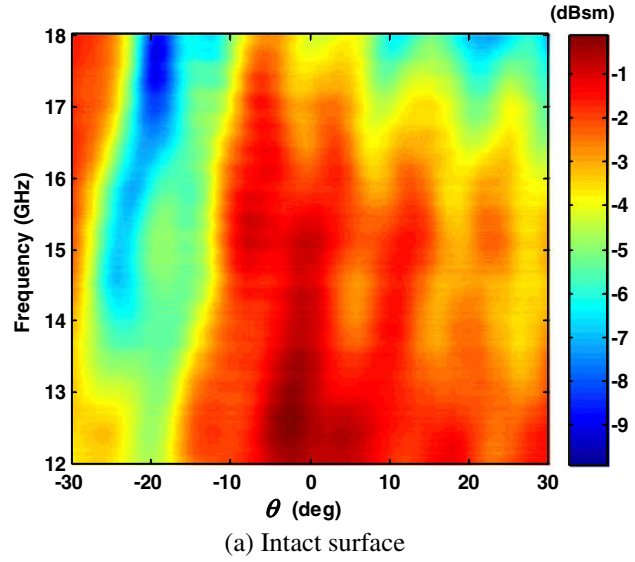

(a) Intact surface

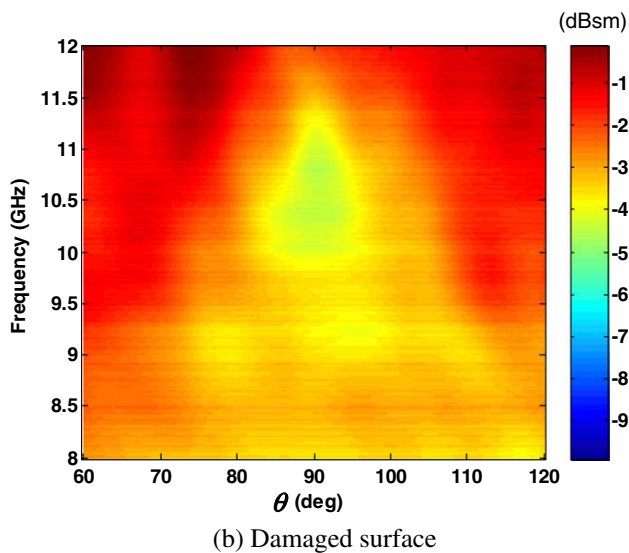(a) Intact surface

(b) Damaged surface
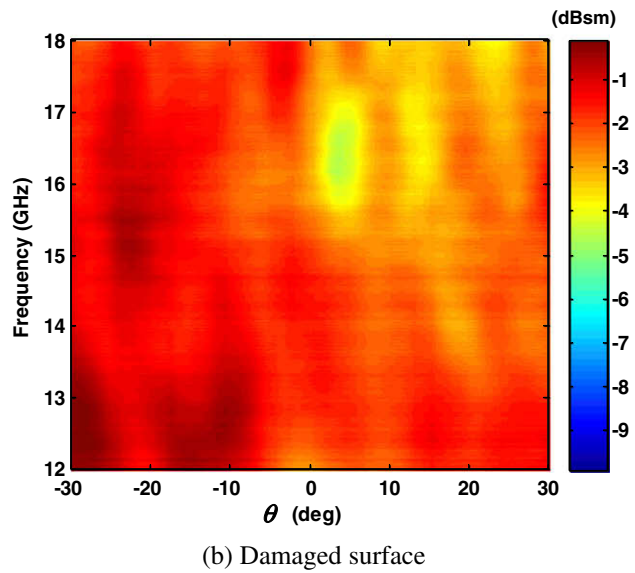
Fig. 9. Frequency–angle data for specimen AD1 measured at normal incidence, Ku-band, HH polarization.

ments at Ku-band also from the specimen AD1. Fig. 10 shows the oblique incidence measurements from the specimen AD1 at X-band. Fig. 11 compares the normal and oblique incidence measurements from the specimen AD2 at X-band. Discussion of these results is provided in Section 6.

5. Image reconstruction

The processing of ISAR measurements can be performed either by frequency-domain or time-domain methods. Frequency-domain methods such as fast Fourier transform (FFT) generally interpolate discrete measurements in frequency-domain and transform the full-bandwidth data into space-domain to obtain the spatial imagery. To achieve required resolutions the processing is

(b) Damaged surface

Fig. 8. Frequency–angle data for specimen AD1 measured at normal incidence, X-band, HH-polarization.
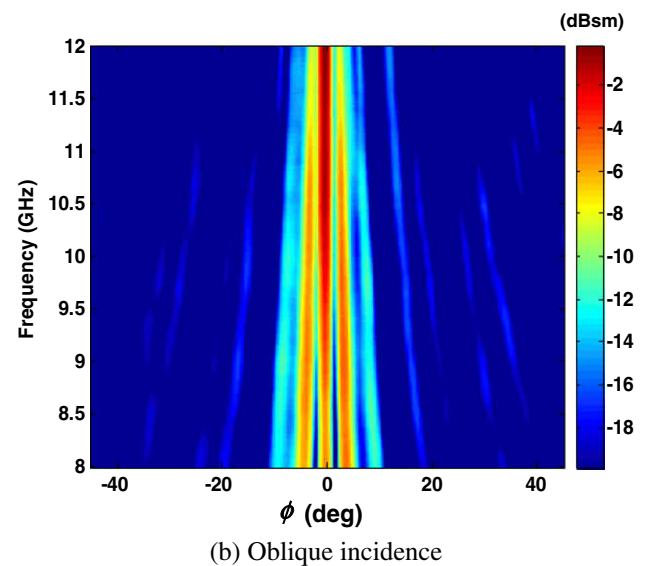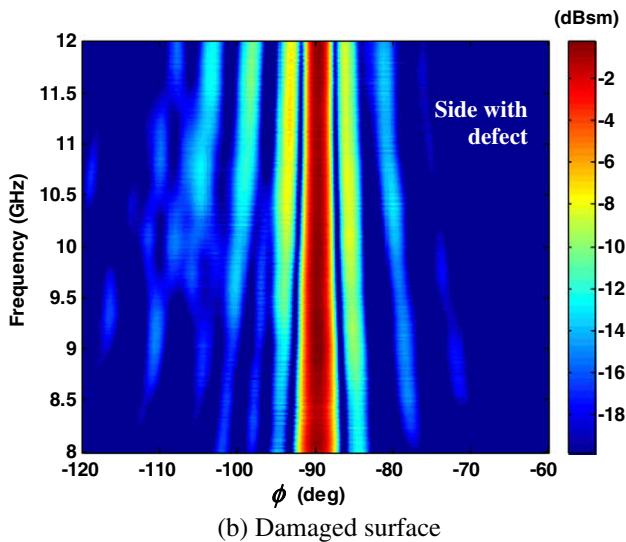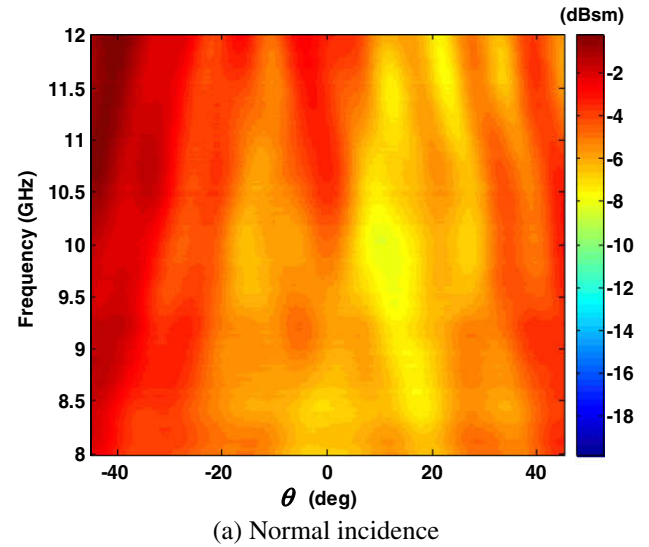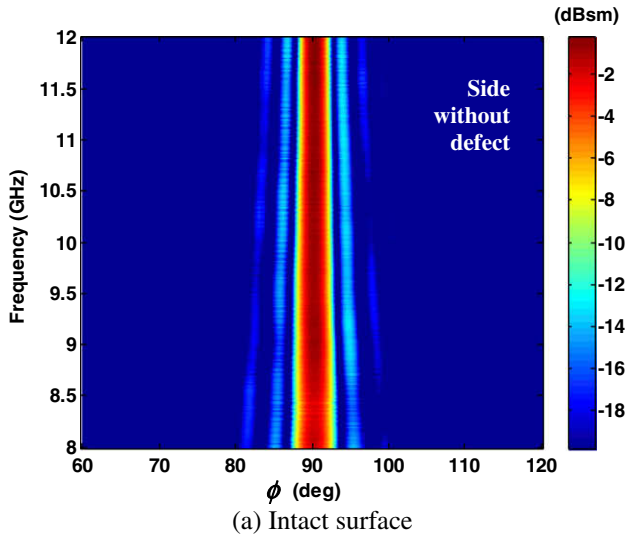
(a) Intact surface

(b) Damaged surface

Fig. 10. Frequency–angle data for specimen AD1 measured at oblique incidence, X-band, HH polarization.

(a) Normal incidence

(b) Oblique incidence

Fig. 11. Frequency–angle data for specimen AD2, X-band, HH-polarization, both damaged surface.

subject to constraints on the frequency bandwidth of and the spacing within the data. Frequency-domain methods are not favored by applications such as real-time imaging and preliminary evaluation on low-resolution images. In addition, interpolation errors in frequency-domain can lead to the wide-spreading artifacts over the entire image.

In view of the constraints of frequency-domain methods, time-domain methods are adopted in this research for processing the data collected by radar NDT. Time-domain methods such as backprojection or tomographic reconstruction algorithm generate an imagery by mapping the Fourier transform of range data back onto a two-dimensional grid. Yegulap [34] proposed an improved (fast) backprojection algorithm that reduces the number of needed computations. In this fast backprojection algorithm the data are first divided into several subapertures and processed to generate relatively-low-resolution images. The final imagery is formed by summing up all the subaperture

images. Consequently, the resolution of images is gradually improved. Such processing scheme can be advantageous for NDT on civil infrastructures, especially when different purposes (e.g. preliminary and detailed inspections) of inspection are needed. The magnitude of an image pixel, $I(\bar{p})$, at position $\bar{p}$ is calculated by the backprojection equation:

$$\begin{aligned} I(\bar{p}) &= \sum_{n=1}^{N_s} I_n(\bar{p}) \\ &= \sum_{n=1}^{N_s} \int_{-l/2}^{l/2} F\left(s_n + \xi, \frac{2}{c}|\bar{p} - \bar{q}(s_n + \xi)|\right) d\xi \end{aligned} \quad (9)$$

where N_s is the number of subapertures, l is the length of subapertures, F is the measurement data received at position $(s_n + \xi)$ and time $(\frac{2}{c}|\bar{p} - \bar{q}(s_n + \xi)|)$, ξ is the distance variable on each subaperture, s_n is the center point of nth subaperture, and $\bar{q}$ is the position vector of aperture points.

Table 1
Summary of the frequency–angle data of specimens AD1 and AD2

		AD1		AD2
		Intact surface	Damaged surface	Damaged surface
Normal incidence	X-band	Fig. 8a	Fig. 8b	Fig. 11a
	Ku-band	Fig. 9a	Fig. 9b	–
Oblique incidence	X-band	Fig. 10a	Fig. 10b	Fig. 11b

Selected images based on the ISAR measurements are reported in the following section.

6. Condition assessment

6.1. Damage detection from the frequency–angle data

Table 1 summarizes the physical radar measurements of specimens AD1 and AD2 in normal and oblique incidence schemes. Comparing Figs. 8a and b it is found that a weak power response area was observed around $\theta = 90$ in the frequency–angle data of damaged surface of specimen AD1 at X-band, where the artificial defect is embedded underneath the GFRP layer. Since the defect region is consisted of Styrofoam whose dielectric constant is smaller than concrete, the reflection response obtained from the defect region is weaker than the one from intact regions. This weak response area suggests the presence of the defect in that location ($\theta = 90$. However, this observation is not reconfirmed by the Ku-band data of specimen AD1 in Figs. 9a and b. The comparison between Figs. 9a and b does not provide sound indication of the presence of defect. The reason is that the signal indicating the presence of defect is much weaker than the specular return in normal incidence scheme. Signals reflecting from the defect are masked by the specular return and cannot be detected in confidence. Same problem also happens to the data of specimen AD2 in Fig. 11a. This suggests the uncertainty of using frequency–angle data in normal incidence scheme for detecting near-surface defects in GFRP–concrete systems.

On the other hand, oblique incidence scheme avoids the difficulties associated with the specular effect. In such incidence scheme the specular effect is only significant when $\varphi = 90$ as the strong reflection response (red[1] region) shown in Fig. 10a. The width of this specular return region depends on the size of horn antenna and the surface smoothness of the specimen. From the comparison between intact and damaged surfaces of specimen AD1 (Figs. 10a and b) the presence of cubic-like defect is indicated by the scattering signals surrounding the specular return region in the frequency–angle data. This indication is consistent, generally, over the entire frequency range in Fig. 10b. When the size of defect changes as the case of specimen AD2 (delamination-like defect), the scattering signals still exist but in different pattern, as shown in

Fig. 11b. The frequency consistency of such indication is also preserved in specimen AD2, suggesting the robustness of oblique incidence scheme for the purpose of damage detection.

6.2. Damage detection based on the backprojection imagery

The ISAR measurements collected from the two representative specimens (AD1 and AD2) in normal and oblique incidence schemes are processed by the fast backprojection
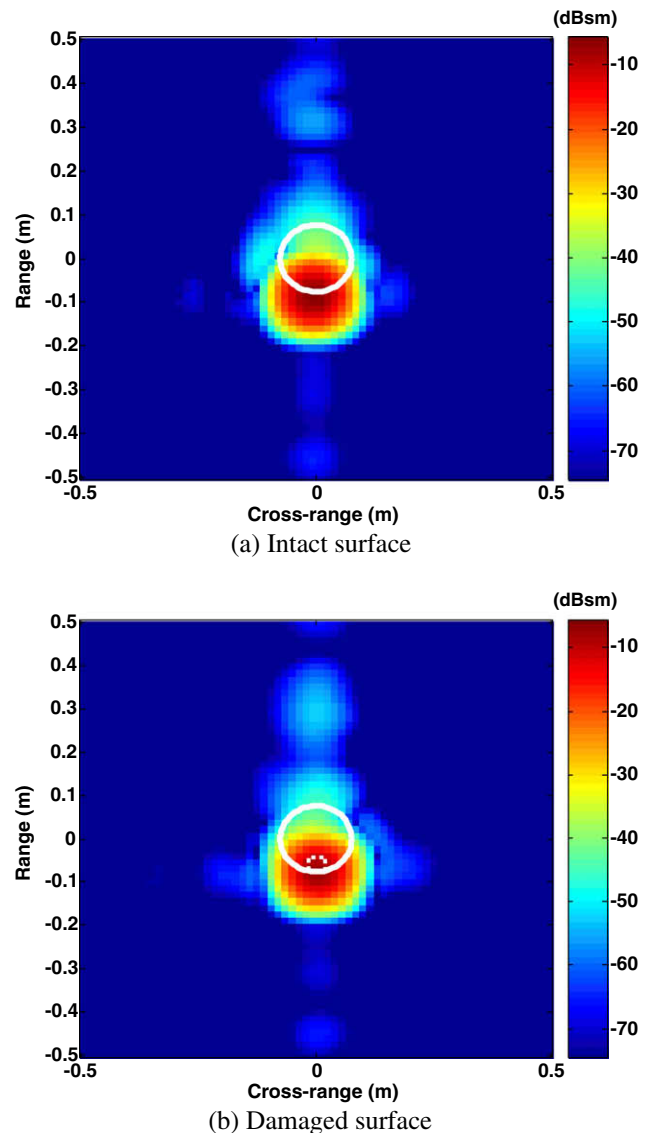

(a) Intact surface

(b) Damaged surface

Fig. 12. Backprojection imagery of specimen AD1, full-bandwidth (8–12 GHz), HH polarization, normal incidence.

---

[1] For interpretation of color in Fig. 10, the reader is referred to the web version of this article.

algorithm. The position of the specimen is indicated by the solid-line and the artificial defect by the dashed-line in Figs. 12–16. Resolutions of the imagery in the range and cross-range axes are 3.72 and 3.76 cm, respectively. The following paragraphs discuss the backprojection images based on the data collected in two measurement schemes (normal and oblique).

6.2.1. Normal incidence scheme

Since the longitudinal axis of the specimen is always perpendicular to the range axis in normal incidence scheme, specular returns dominate the response at all measurement angles. Fig. 12a and b shows the backprojection images of intact and damaged surfaces of specimen AD1 in normal
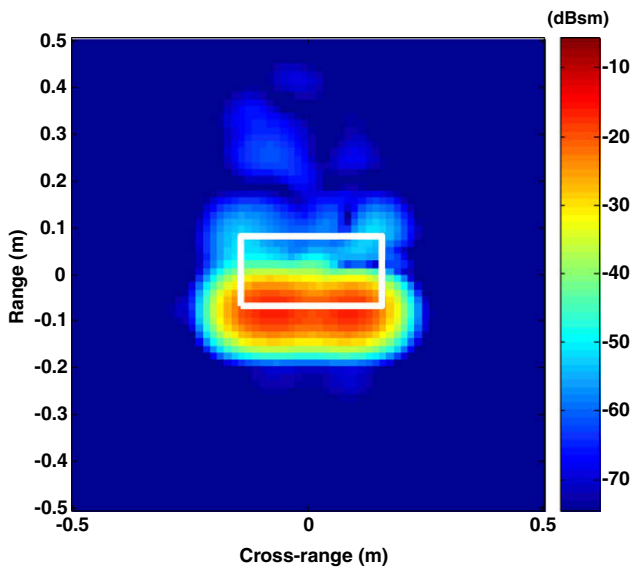

Fig. 15. Backprojection imagery of specimen AD1, damaged surface, oblique incidence ($\varphi = 100°$), full-bandwidth (8–12 GHz).
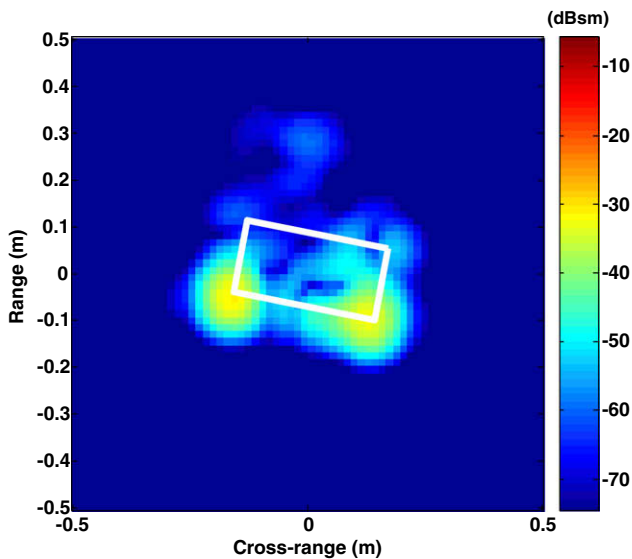

Fig. 13. Backprojection imagery of specimen AD1, intact surface, oblique incidence ($\varphi = 90°$), full-bandwidth (8–12 GHz).

Fig. 16. Backprojection imagery of specimen AD2, damaged surface, oblique incidence ($\varphi = 100°$), full-bandwidth (8–12 GHz).

Fig. 14. Backprojection imagery of specimen AD1, intact surface, oblique incidence ($\varphi = 100°$), full-bandwidth (8–12 GHz).

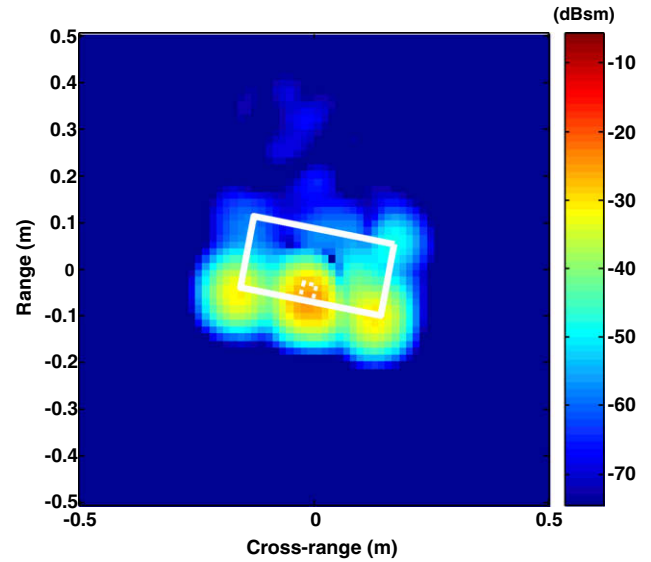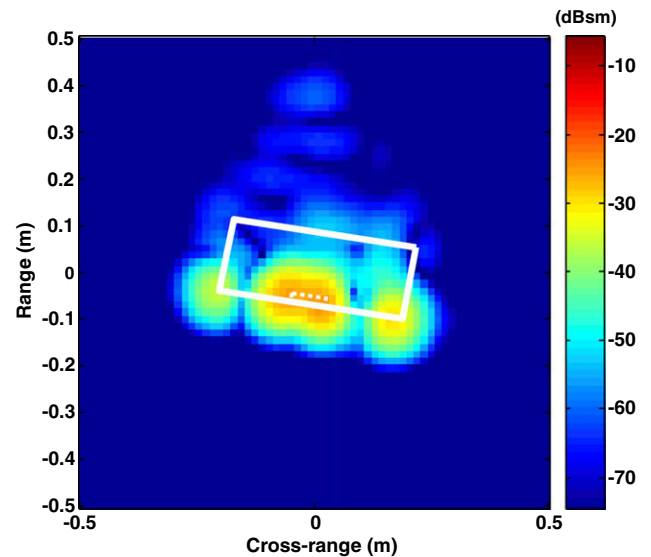incidence scheme at 90° (the defect is normally facing the antenna). Peak response occurs at the front-surface of the specimen where the transmitted EM waves first encounter the specimen, as shown in Fig. 12. The peak responses are −6.8468 dBsm (decibel per square meter) for intact surface and −7.6289 dBsm for damaged surface, both of specimen AD1. The comparison between Fig. 12a and b suggests that the difference between the intact and artificially damaged surfaces is insignificant, although the area of the defect is more than 1.25 cm-by-1.25 cm. The comparison between the intact and AD2 specimens also provides similar observation. Therefore, it is suggested that normal incidence scheme is not suitable for detecting near-surface defects in this FAR NDT technique.

6.2.2. Oblique incidence scheme

In oblique incidence scheme the problem with specular return is avoided by tilting the specimen at various angles, meaning that the longitudinal axis of the specimen is no longer always perpendicular to the range axis of the antenna but only at one angle ($\varphi = 90°$). This case is demonstrated in Fig. 13 using the intact surface of specimen AD1 as an example. It is clearly seen that in Fig. 13 specular returns occur from the outer surface of the specimen and cover the scattering signal of the defect if there is any.

Specular returns are eliminated or reduced when the specimen is not perpendicular to the range axis of the antenna. Fig. 14 shows the backprojection image of intact specimen tilted at 10. In Fig. 14 only the specular returns from the two ends of the specimen remain (the cap effect). The response between the two ends should be zero if the surface of the specimen is perfectly smooth. Since this is not the case for the GFRP–concrete specimens used in this study (the surface of GFRP sheet is not perfectly smooth), some minor response between the two ends of the intact specimen is noticed in Fig. 14.

Fig. 15 shows the backprojection image of specimen AD1 (cubic defect) tilted at 10°. An obvious scattering signature between the two ends is found in Fig. 15. This scattering signature clearly indicates the presence of the artificial defect, and is centered at the location where the defect is placed. In the case of specimen AD2 (delamination) similar conclusion can be drawn from Fig. 16. The area of the scattering signature is also related to the size of the defect as seen when comparing Fig. 15 with Fig. 16.

In view of the evidences mentioned above, the authors believe that this scattering signature can be used for indicating the presence, locating the position, and quantifying the size of near-surface defects of GFRP–concrete cylindrical structures. It is also noteworthy that the interference from the two ends will diminish in real structures, making this technique even more powerful and attractive for practical applications.

7. Research needs for future development

The performance of this proposed FAR NDT technique has been demonstrated by laboratory radar measurements on artificially damaged specimens, along with the use of image reconstruction algorithm. However, further exploration of several research issues, before the practical application of this technique, is still required. These issues are summarized in the following.

7.1. Dielectric properties of cementitious materials

NDT techniques using radar rely on the knowledge of dielectric/electromagnetic properties of materials. While many materials have been well-studied electromagnetically, cementitious materials are still under investigation with difficulties in dielectric modeling, due to the heterogeneity of their structure and the time-dependent behavior of various

phases in the material. It is essential that thorough knowledge on the dielectric properties of cementitious materials are developed for reliable use of radar NDT techniques for civil infrastructures.

7.2. Numerical simulation capability

Three-dimensional simulation of EM propagation and reflection is needed as a parallel approach to experimental investigation. Such capability can be utilized for parametric study leading to extensive data than what could be measured in laboratory.

7.3. Field measurements and signal de-noising algorithm

The concept of the proposed FAR NDT technique has been validated based on the laboratory measurements from scaled, artificially damaged specimens. When applied to real structures other issues such as the configuration of experimental set-up need to be addressed. On-site measurement set-up must be optimized to account for the variations in different situations.

There is also a need to evaluate the performance of the proposed technique by noise-contaminated signals. It is realized that the findings summarized in this paper are based on the preliminary experimental work conducted in a laboratory facility in which potential noises are *a priori* prevented. Signals collected from real structures in open spaces are usually contaminated by natural and manmade noises. Should the noise level exceed the detectability of actual signal the performance of image reconstruction algorithm will be hampered. Noises must be removed from or reduced in the measurements collected from actual structures before any further processing for condition assessment. Filtering techniques based on compact supported (e.g. wavelets) and non-compact supported (e.g. sinusoidal) basis can be used for the separation of noise and signal in transient and steady-state responses.

8. Conclusion

A far-field airborne radar (FAR) NDT technique aiming at the damage detection in the near-surface region of GFRP-wrapped concrete structures is proposed. To validate the feasibility of the technique physical radar measurements were performed. Physical radar measurements on GFRP-wrapped concrete cylinder specimens with artificially introduced air voids and delamination behind the GFRP layer were collected at X- and Ku-band in a compact/RCS antenna facility. The radar antenna operated in ISAR mode providing reflection measurements at different angles. Two measurement schemes, normal incidence and oblique incidence, were investigated.

It is found that in the normal incidence measurements, due to the specular effect, the difference in the power responses between intact and damaged regions is not constantly significant. On the other hand, the oblique inci-

dence measurements provide a clear indication on the presence of the defect in the frequency–angle imagery. Measurements at oblique incidence provided superior damage indication than those at normal incidence case, regardless of wave polarization and the thickness of the defect. Surface condition of the specimen such as roughness, affects the reflected power measurements in higher frequency ranges (Ku-band), suggesting the importance of data de-noising and filtering.

In this development the use of backprojection algorithm for processing frequency–angle data into range–cross-range imagery provides clear indication of the presence and location of defects in two artificially damaged specimens (AD1 and AD2). From the measurement and imaging results it is found that oblique measurement scheme appears to be effective and robust on detecting GFRP debonding. Artificial damages can be detected and located with the developed imaging capability. It is shown that the proposed FAR NDT technique has potential in identifying near-surface damages (GFRP delamination, concrete cracking) behind the GFRP layer by the far-field radar measurements. Further work is underway for radar measurements and numerical simulation of mechanically damaged specimens, and data de-noising and filtering for signal processing.

Acknowledgements

References

[1] ACI-440 Committee. Guide for the design and construction of externally bonded FRP systems for strengthening concrete structures. ACI-440.2R-02. Farmington Hills: American Concrete Institute, 2002.

[2] Au C, Büyüköztürk O. Effect of fiber orientation and ply mix on fiber reinforced polymer-confined concrete. J Compos Constr 2005;9(5):397–407.

[3] Nanni A. Fiber-reinforced-plastic (FRP) reinforcement for concrete structures: properties and applications. Amsterdam: Elsevier; 1993.

[4] Priestley MJN, Seible F. Seismic design and retrofit of bridges. New York: Wiley; 1996.

[5] Sheikh SA, Yau G. Seismic behaviour of concrete columns confined with steel and fibre reinforced polymers. ACI Struct J 2002;99(1):72–80.

[6] Howie I, Karbhari VM. Effect of tow sheet composite wrap architecture on strengthening of concrete due to confinement: I – experimental studies. J Reinf Plast Compos 1995;14:1008–30.

[7] Karbhari VM, Eckel DA, Tunis GC. Strengthening of concrete column stubs through resin infused composite wraps. J Thermoplast Compos Mater 1993;6:92–106.

[8] Nanni A, Bradford NM. FRP jacketed concrete under uniaxial compression. Constr Build Mater 1995;9(2):115–24.

[9] Popovics JS, Rose JL. Survey of developments in ultrasonic NDE of concrete. IEEE Trans Ultrason Ferroelectr Freq Control 1994;41(1):140–3.

[10] Tanigawa Y, Yamada K, Kiriyama S. Frequency characteristics of AE in concrete. Proc JCI 1997;2:129–32.

[11] Büyüköztürk O. Imaging of concrete structures. NDT&E Int 1998;31(4):233–43.

[12] Mirmiran A, Shahawy M, Echary HE. Acoustic emission monitoring of hybrid FRP–concrete columns. J Eng Mech 1999;125(8):899–905.

[13] Mirmiran A, Wei Y. Damage assessment of FRP-encased concrete using ultrasonic pulse velocity. J Eng Mech 2001;127(2):126–35.

[14] Bastianini F, Tommaso AD, Pascale G. Ultrasonic non-destructive assessment of bonding defects in composite structural strengthenings. Compos Struct 2001;53(4):463–7.

[15] Feng MQ, Flaviis FD, Kim YJ. Use of microwaves for damage detection of fiber reinforced polymer-wrapped concrete structures. J Eng Mech 2002;128(2):172–83.

[16] Starnes MA, Carino NJ, Kausel EA. Preliminary thermography studies for quality control of concrete structures strengthened with fiber-reinforced polymer composites. J Mater Civ Eng 2003;15(3):266–73.

[17] Hillger W. Inspection of concrete by ultrasonic testing. In: Proceedings of the 4th European conference on non-destructive testing, London, vol. 2; 1987. p. 1003–12.

[18] de Vekey RC. Non-destructive evaluation of structural concrete: a review of European practice and developments. In: Proceedings of nondestructive evaluation of civil structures and materials. Boulder: National Science Foundation and University of Colorado; 1990.

[19] Malhotra VM, Carino NJ. CRC handbook on nondestructive testing of concrete. Boca Raton: CRC Press; 1991.

[20] Fenning PJ, Brown AJ. Ground penetrating radar investigation. Constr Repair 1995;9(6):17–21.

[21] Mellet JS. Ground penetrating radar applications in engineering, environmental management, and geology. J Appl Geophys 1995;33:157–66.

[22] Saarenketo T, Scullion T. Road evaluation with ground penetrating radar. J Appl Geophys 2000;43:119–38.

[23] Clemena GG. Short-pulse radar methods. In: Malhotra VM, Carino NJ, editors. CRC handbook on nondestructive testing of concrete. Boca Raton: CRC Press; 1991. p. 253–74.

[24] Büyüköztürk O, Rhim HC. Electromagnetic properties of concrete at microwave frequency range. ACI Mater J 1998;95(3):262–71.

[25] Akuthota B, Hughes D, Zoughi R, Myers J, Nanni A. Near-field microwave detection of disbond in carbon fiber reinforced polymer composites used for strengthening cement-based structures and disbond repair verification. J Mater Civ Eng 2004;16(6):540–6.

[26] Huston D, Hu JQ, Maser K, Weedon W, Adam C. GIMA ground penetrating radar system for monitoring concrete bridge decks. J Appl Geophys 2000;43:139–46.

[27] Wehner DR. High resolution radar. Norwood: Artech House; 1987.

[28] Eaves JL, Reedy EK. Principles of modern radar. New York: Van Nostrand Reinhold; 1987.

[29] Mensa DL. High resolution radar cross-section imaging. Norwood: Artech House; 1991.

[30] Skolnik MI. Radar handbook. New York: McGraw-Hill; 1990.

[31] Balanis CA. Antenna theory: analysis and design. New York: John Wiley & Sons; 1997.

[32] Knott EF, Shaeffer JF, Tuley MT. Radar cross section. Norwood: Artech House; 1993.

[33] Büyüköztürk O, Yu T-Y, Ortega JA. A methodology for determining complex permittivity of construction materials based on transmission-only coherent, wide-bandwidth free-space measurements. Cem Conc Compos 2006;28(4):349–59.

[34] Yegulalp AF. Fast backprojection algorithm for synthetic aperture radar. In: Proceedings of IEEE radar conference; 1999. p. 60–5.